

Advanced durable ceramic-polymer ultra-superhydrophobic coating with anti-icing, anti-vapor condensation, and corrosion-resistant properties

Khaskhoussi, Amani; Rahimi, Ehsan; Calabrese, Luigi; Cornet, Arjan; Anusuyadevi, Prasaanth Ravi; Gonugunta, Prasad; Mol, Arjan; Proverbio, Edoardo

DOI

10.1016/j.cej.2025.163767

Publication date 2025

Document VersionFinal published version

Published in Chemical Engineering Journal

Citation (APA)

Khaskhoussi, A., Rahimi, E., Calabrese, L., Cornet, A., Anusuyadevi, P. R., Gonugunta, P., Mol, A., & Proverbio, E. (2025). Advanced durable ceramic-polymer ultra-superhydrophobic coating with anti-icing, anti-vapor condensation, and corrosion-resistant properties. *Chemical Engineering Journal*, *515*, Article 163767. https://doi.org/10.1016/j.cej.2025.163767

Important note

To cite this publication, please use the final published version (if applicable). Please check the document version above.

Copyright

Other than for strictly personal use, it is not permitted to download, forward or distribute the text or part of it, without the consent of the author(s) and/or copyright holder(s), unless the work is under an open content license such as Creative Commons.

Takedown policy

Please contact us and provide details if you believe this document breaches copyrights. We will remove access to the work immediately and investigate your claim.

ELSEVIER

Contents lists available at ScienceDirect

Chemical Engineering Journal

journal homepage: www.elsevier.com/locate/cej



Advanced durable ceramic-polymer ultra-superhydrophobic coating with anti-icing, anti-vapor condensation, and corrosion-resistant properties

Amani Khaskhoussi ^{a,*} ^o, Ehsan Rahimi ^{b,*} ^o, Luigi Calabrese ^a, Arjan Cornet ^b ^o, Prasaanth Ravi Anusuyadevi ^b ^o, Prasad Gonugunta ^b ^o, Arjan Mol ^b ^o, Edoardo Proverbio ^a ^o

ARTICLE INFO

Keywords: Ultra superhydrophobic Ceramic-polymer coating Anti-icing Corrosion protection Anti-vapor condensation

ABSTRACT

We present a mechanically robust, cost-effective, and scalable ultra-superhydrophobic ceramic-polymer composite coating featuring a hierarchical micro/nano-structured surface. This advanced coating, fabricated via a single-step process, integrates alumina (Al₂O₃) and zirconia (ZrO₂) to harness their individual and synergistic effects, achieving an extreme water contact angle of 180° and a sliding angle of 1°. The coating demonstrates strong adhesion and compatibility with a wide range of substrates, including aluminum and concrete. The Al₂O₃–ZrO₂-based composite exhibits outstanding physicochemical properties, including superhydrophobicity, anti-icing, anti-corrosion, and anti-vapor condensation capabilities. It also maintains excellent non-wetting behavior across a variety of liquids. Comprehensive surface analyses, encompassing microstructural, morphological, and chemical characterization, underscore the critical role of hierarchical structuring and tailored surface chemistry in enhancing functionality. Mechanical durability assessments reveal that the coating retains its superhydrophobic performance even after extensive scratching test. Moreover, it exhibits self-cleaning, anti-adhesion, and anti-fouling characteristics, attributed to its engineered surface texture and the synergistic contributions of Al₂O₃–ZrO₂ heterojunctions and oxide-silane bonding (Si–O–Si and Si–OH). This multifunctional ceramic-polymer coating addresses key challenges in large-scale deployment by offering a streamlined, scalable fabrication method and versatile performance, positioning it as a promising solution for diverse industrial applications.

1. Introduction

The accumulation and adhesion of water and ice on solid surfaces pose significant challenges across various industries, including construction, aviation, marine transportation, and renewable energy [1,2]. Ice accretion on infrastructure, such as power lines, aircraft, and wind turbines, can lead to aerodynamic instability, reduced efficiency, and ultimately increase maintenance costs [3–5]. Addressing these issues requires effective strategies that optimize performance, sustainability, and economic feasibility. Conventionally, strategies for preventing ice accumulation are categorized into active and passive methods [6–8]. Active techniques, such as mechanical removal and thermal de-icing, are energy-intensive and often rely on environmentally hazardous chemicals [9,10]. Passive methods, including low-surface-energy coatings, seek to prevent ice accumulation but often suffer from limited durability and mechanical robustness [11,12]. These limitations highlight the need

for more durable, low-maintenance solutions that can effectively mitigate water and ice adhesion. Superhydrophobic surfaces have emerged as a promising approach due to their ability to repel water, with contact angles exceeding 150° and sliding angles below 10° [13]. Inspired by natural examples like lotus leaves, these surfaces utilize a combination of low surface energy and hierarchical micro- and nanoscale roughness to minimize contact with water, allowing droplets to roll off easily. This unique morphology not only prevents water from adhering before freezing but also delays icing and reduces ice adhesion while maintaining surface cleanliness [13,14].

However, the application of superhydrophobic surface treatments for anti-icing purposes poses significant technical limitations. The transition from the Cassie-Baxter state, where air pockets prevent water penetration, to the Wenzel state, where water infiltrates surface roughness, increases ice adhesion [15,16]. Repeated icing and de-icing cycles degrade surface structures, ultimately compromising long-term

E-mail addresses: khaskhoussiamani105@gmail.com (A. Khaskhoussi), e.rahimi-2@tudelft.nl (E. Rahimi).

^a Department of Engineering, University of Messina, Contrada di Dio Sant'Agata, 98166 Messina, Italy

b Delft University of Technology, Department of Materials Science and Engineering, Mekelweg 2, Delft 2628 CD , the Netherlands

^{*} Corresponding authors.

performance [17]. These issues emphasize the need for mechanically robust and durable superhydrophobic coatings to ensure long-term effectiveness. Ruan et al. [18] stated that the choice of experimental parameters during the fabrication process plays a crucial role in determining surface properties and, in turn, the superhydrophobic behavior of materials. For example, Chen et al. [19] demonstrated that chemical etching time directly affects the transition in wettability of aluminum surfaces from hydrophilic to hydrophobic. Similarly, Shi et al. [20] employed a two-step method to create a superhydrophobic aluminum surface, first using hydrothermal treatment to develop a flower-like hierarchical structure, followed by lauric acid treatment to lower surface energy. These studies underscore the need to optimize fabrication parameters for achieving desirable superhydrophobic properties.

In addition to anti-icing, superhydrophobic surfaces exhibit excellent potential for corrosion inhibition. Dou et al. [21] observed that copper superhydrophobic surfaces enhanced corrosion resistance by more than 102 times in marine environments. Likewise, Li et al. [22] demonstrated that superhydrophobic surfaces on 6061 aluminum alloy exhibited a corrosion resistance efficiency of about 76 % in comparison to hydrophobic surfaces. Feng et al. [23] further demonstrated that superhydrophobic coatings with water contact angles (WCA) above 156° and sliding angles around 3° provide long-term corrosion resistance on aluminum alloys. An effective strategy for enhancing superhydrophobicity involves the deposition of self-assembled silane monolayers on surfaces. Prior literature [22,24-29] suggests that selfassembled monolayers significantly reduce surface energy while improving hydrophobicity. This approach is advantageous due to its ability to produce well-defined, highly ordered structures with minimal processing complexity. Particularly, alkylsilane-based self-assembled monolayers exhibit strong siloxane bonding, which ensures mechanical and chemical stability [23,30,31]. These properties make them suitable for various applications, including wear protection, corrosion prevention, and chemical sensing. Despite these advancements, existing fabrication methods face challenges such as multi-step processes, high costs, and reliance on environmentally harmful chemicals like fluorinated compounds. Ruan et al. [18] emphasized the need for costeffective and environmentally friendly techniques to overcome these barriers and enable the large-scale application of superhydrophobic surfaces. Other applications of superhydrophobic surfaces include rapid oil-water separation [32,33], efficient solar evaporator with antibacterial properties [34], a thermally stable superhydrophobic surface [35], and photocatalytic self-cleaning capabilities [36].

This study explores the development of a mechanically robust, costeffective, and scalable ceramic-polymer ultrasuperhydrophobic coating with a hierarchical micro-nano structure. The coating is fabricated through a single-step process and is designed for compatibility with various substrates, including aluminum and concrete (Available in Movies S1 and S2). The research investigates the role of alumina (Al₂O₃) and zirconia (ZrO2) in influencing the coating's structural and chemical properties, with a particular focus on Al-O/Zr-O heterojunctions and siloxane (Si-O-Si) bonding. Alumina (Al₂O₃) and zirconia (ZrO₂) were selected as key components of the coating due to their synergistic properties that are well-suited for ultra-superhydrophobic and anti-icing applications. Al₂O₃ contributes high hardness and excellent wear resistance [37], which helps preserve the micro/nanostructure under mechanical abrasion. In contrast, ZrO2 offers superior fracture toughness and crack resistance [38], which enhances the structural integrity of the coating during repeated icing and de-icing cycles. Both oxides exhibit high thermal stability and chemical inertness, ensuring durability under extreme environmental conditions such as temperature fluctuations, humidity, and UV exposure [39,40]. Furthermore, the distinct particle morphologies of Al₂O₃ and ZrO₂ facilitate the formation of a hierarchical surface architecture essential for achieving the Cassie-Baxter wetting regime and minimizing ice adhesion [41]. Together, these materials enable the fabrication of a robust, thermally stable, and environmentally resilient coating optimized for long-term anti-icing

performance.

To understand the mechanisms underlying its performance, this study examines the coating's interaction with water, hot vapor, and ice, focusing on its resistance to vapor condensation, anti-icing behavior, and long-term chemical durability, including anti-corrosion performance. Durability assessments further evaluate its chemical stability and functionalities under aggressive chloride-containing environments. This approach addresses key challenges in scalability and fabrication, offering insights into the development of multifunctional coatings for water, vapor, and ice-related applications. While this study focuses on experimental observations of the coating's performance under cyclic ice shear testing, it does not include theoretical analysis of the underlying mechanisms. Future work will aim to incorporate theoretical modeling to further explore the interfacial behavior during repeated ice adhesion and detachment cycles.

2. Experimental procedure

2.1. Materials and reagents

An aluminum alloy as substrate (30 mm \times 24 mm \times 2 mm) was obtained from a 1000 mm \times 1000 mm \times 2 mm as received laminated plate made of the commercially available EN AW6082-T6 aluminum alloy (nominal chemical composition Si 0.70–1.3 wt%; Mg 0.60–1.2 wt %; Fe \leq 0.50 wt%; Cu \leq 0.10 wt%; Mn 0.40–1.0 wt%; Cr \leq 0.25 wt%; Zn \leq 0.20 wt%; Ti \leq 0.10 wt%; Al balance). This alloy is widely used in machining, offshore, or transport applications. Octadecyltrimethoxysilane (C21H46O3Si, 99 %) was purchased from Sigma-Aldrich, St. Louis, MO, USA. Silanol-terminated polydimethylsiloxane, PDMS, M.W. 18,0000, Viscosity at 25 °C, 700–800 cSt, CAS: 70131–67-8 compounds, was supplied by Gelest (Morrisville, USA). Detailed information on the micro and nanopowders of alumina (Al2O3) and zirconia (ZrO2) used in the fabrication of superhydrophobic coating is provided in Table 1.

2.2. Preparation of various superhydrophobic coatings

All aluminum substrates, with a root mean square surface roughness of Rq $=269\pm50$ nm (analyzed by AFM in section 2.5) were cleaned using the following procedure: ultrasonic cleaning in acetone, ultra-pure water, and ethanol, and finally drying at room temperature in a silica-gel dryer. The coating suspension was prepared by adding poly-dimethylsiloxane (PDMS) and silane to ethanol (weight ratio 1:4:15) at room temperature, with vigorous stirring for 30 min. Both the nano-powder and micropowder of the selected oxides were added gradually in equal amounts to the prepared suspension. The mixture was then mechanically stirred for 10 min, followed by ultrasonication for an additional 10 min. The coating suspension was then applied to the aluminum substrate using a dipping process. Finally, the samples were dried at room temperature for 30 min to allow solvent evaporation, followed by curing at 200 $^{\circ}\text{C}$ for 2 h.

2.3. Wettability and surface energy analyses

The WCA's of the coatings were measured using an Attension Theta Tensiometer (Attension, Biolin Scientific, Gothenburg, Sweden) provided by Biolin Scientific, following the sessile drop technique. A

 Table 1

 Detailed information related to the micro- and nano-sized oxide particles.

Oxides	Particle size	Purity (%)	CAS number	Product suppliers
ZrO_2	0.9–1.1 μm	99.5 %	1314-23-4	Alfa Aesar
	40-50 nm	99.5 %	1314-23-4	IOLITEC nanomaterials
Al_2O_3	0.9–1.1 μm	99.9 %	1344-28-1	Alfa Aesar
	40–50 nm	99.5 %	1344-28-1	Alfa Aesar

distilled water droplet of 3 μL was placed on the sample surface at room temperature. A micro charged-coupled device (CCD) camera (Attension, Biolin Scientific) on-site recorded images of the droplets, which were subsequently analyzed using the PC Attension software (OneAttension V. 2.3) to obtain the static contact angles of the droplets on each of the coatings. Fifty WCA measurements were taken per sample on a regular grid. The surface free energy (SFE) was calculated using the OWRK formula (Equation (1)), based on the contact angle measurements of water and three other aprotic liquids with known surface tensions: glycerol and ethylene glycol, which are polar liquids, and diiodomethane, a non-polar liquid.

$$\gamma_{sl} = \gamma_s + \gamma_l - 2(\gamma_s^d \gamma_l^d)^{0.5} - 2(\gamma_s^p \gamma_l^p)^{0.5}$$
 (1)

where γ_s^d and γ_l^d are the dispersive components and γ_s^p and γ_l^p are the polar components of the surface tension for liquids and solid phases.

2.4. Chemical surface characterization by XPS

The chemical bonding information of the coating materials on the metal substrates was analyzed in this work through X-ray photoelectron spectroscopy (XPS). Metal substrates with appropriate coatings of size 1 \times 1 cm² were carefully loaded inside the ESCA 5400 system (supplied by Physical Electronics, INC. (PHI)), equipped with an Aluminium (Al) Kα X-ray nonmonochromatic source (hv = 1486.7 eV). During the analysis, the vacuum inside the XPS system was maintained at around 10⁻⁹ mbar. All specimens were analyzed on a circular scanning area with a diameter of 0.4 mm, and the analysis depth ranged from 3 to 5 nm. The settings of the instrument during the full survey measurement were 89.45 eV pass energy and 0.5 eV resolution. Subsequently, during high-resolution multiplex scans, measurements were carried out at 0.2 eV resolution with 71.55 eV pass energy. The take-off angle for both the full survey and high-resolution measurement was set at 45°. The resultant spectra from the XPS instrument were processed using the MultiPak version 8.0 software supplied by Physical Electronics Inc. To counterbalance the charging of the specimen studied during the XPS analysis, all the highresolution spectra were adjusted through carbon shift (by referencing the C-C peak of the C1s spectrum at 284.8 eV). Subsequently, curve fitting of the XPS data was performed.

2.5. Microstructural, morphological, and surface potential/charge characterizations

The micro- and nano-scale structural features present across all coatings were systematically characterized using Field Emission Scanning Electron Microscopy (FE-SEM, JEOL JSM-6500F) equipped with an energy-dispersive X-ray spectrometer (EDXS). High-resolution images were acquired at an acceleration voltage of 5 kV with working distances of 10 mm and 25 mm. The cross-sectional morphology of all coatings was analyzed using a Thermo ScientificTM HeliosTM UXe DualBeam G4 scanning electron microscope. This advanced instrument, equipped with an EDXS detector and a Focused Ion Beam (FIB), utilized FIB milling to facilitate precise cross-sectional imaging of the coated specimens in conjunction with SEM. Surface characterization, including topography, amplitude signals (derived from cantilever oscillation amplitudes), and surface potential or charge distribution, was conducted through atomic force microscopy (AFM) and scanning Kelvin probe force microscopy (SKPFM). The AFM measurements were performed using a Bruker Dimension EdgeTM system with an n-type doped silicon pyramid singlecrystal tip coated with PtIr5 (SCM-Pit probe), featuring a tip radius of 20 nm and a height of $10-15 \mu m$. The initial scan, performed in tapping mode, captured surface topography and amplitude signals. For SKPFM analysis, a subsequent backward scan involved lifting the AFM tip to a height of 100 nm, enabling surface potential and charge distribution measurements based on the topographical data recorded during the first scan. The 100 nm lift was chosen to minimize the influence of local

surface topography heterogeneities on the potential signals. AFM and SKPFM imaging were performed under ambient conditions (temperature: $23\,^{\circ}$ C, relative humidity: \sim 42 %). All images had a pixel resolution of 512×512 and were acquired at a scan frequency of 0.3 Hz.

2.6. Anti-icing and vapor condensation properties

The anti-icing properties were evaluated by shear stress analysis performed with a custom-built mold using a universal testing machine (Lloyd EZ 50). Anti-icing test specimens included uncoated (bare aluminum alloy) and $Al_2O_3 - ZrO_2$ polymer coating samples, which were frozen in a mold containing 40 ml of deionized water at $-19\,^{\circ}\mathrm{C}$ for 48 h. Afterward, the mold was fixed in the universal testing machine, and the sample was extracted from the ice at a speed of 3 mm/min. The force (F) required to detach the sample from the mold was recorded and converted into shear stress. The shear stress was calculated as the average of three tests carried out on three different specimens.

Ice adhesion properties were evaluated by shear stress analysis. The experiment was carried out in less than 30 s in a conditioned environment (T: 20 °C; Humidity: 46 %). The peak force F needed to detach the ice from the sample was registered. The ice adhesion strength (τ) in shear can be calculated by:

$$\tau = F/A \tag{2}$$

where A is the surface of the specimen in contact with the ice. The shear stresses were calculated as the average of three tests carried out on three different specimens for each treatment [42,43].

2.7. Experimental vapor condensation process

The vapor condensation experiment was conducted within a sealed chamber containing a beaker of heated water to generate water vapor. The chamber environment was allowed to equilibrate until it reached 100 % relative humidity, ensuring a fully saturated vapor atmosphere. Two sample types were placed inside the chamber: a bare aluminium substrate and a substrate coated with an $\rm Al_2O_3-\rm ZrO_2$ polymer composite. Both samples were positioned to face the saturated vapor directly, allowing for uniform exposure. The condensation behavior on each surface was carefully monitored and compared to evaluate differences in nucleation and droplet formation characteristics.

2.8. Electrochemical and corrosion protection behavior assessments

The electrochemical response and corrosion protective behavior of $Al_2O_3 - ZrO_2$ polymer coating (Ultra superhydrophobic coating) was studied in a 3.5 wt% NaCl solution as a corrosive environment at room temperature and pH \sim 7. The electrochemical measurements were performed utilizing a computer-controlled potentiostat BioLogicSP-300 in a conventional three-electrode electrochemical cell in which Ag/ AgCl/KCL_{sat}, a platinum plate, and ultra superhydrophobic coating were reference, counter, and working electrodes, respectively. Potentiodynamic polarization (PDP) was conducted to determine the corrosion potential (Ecorr) and corrosion current density (icorr) of the coated and bare aluminium alloy substrate. The PDP curves were recorded with a scanning rate of 1 mV/s from the -100 mV vs. open circuit potential (OCP) for the cathodic branch and extending to +250 mV vs. OCP for the anodic branch. Prior to the PDP test, both the bare and coated aluminum alloy were exposed to the electrolyte for 30 min to ensure a steady state condition at a stable OCP. The long-term corrosion potential and WCA of the ultra-superhydrophobic coating were monitored for 1 year by tracking corrosion potential versus time to evaluate its (electro)chemical stability.

3. Results and discussion

3.1. Surface microstructural and chemical composition

The mixture was prepared by combining organosilicon compounds, a blend of silanol-terminated PDMS and octadecyltrimethoxysilane (OTMS), with micro- and nano-powders of Al_2O_3 , ZrO_2 , or their combination ($Al_2O_3 + ZrO_2$). This process resulted in a heterogeneous composite coating with a varied distribution of oxide particles on the AA6082-T6 substrate, as shown in Fig. 1a and 1b. The three coatings studied included: (1) $Al_2O_3 + ZrO_2 +$ organosilicon polymer, (2) $ZrO_2 +$ polymer, and (3) $Al_2O_3 +$ polymer. Among these, the first coating demonstrated the highest superhydrophobic performance with a hierarchical micro-nano structure (high-magnified SEM images in Fig. S1). To understand the underlying reasons for this performance, we conducted a systematic analysis of the coating surface and bulk structure. SEM and EDX imaging (Figs. S2, S3, and S4) confirmed the presence of both micro- and nano-sized powders, as well as the expected elemental composition corresponding to the coating formulation.

The cross-sectional analysis of the bulk composition of the coatings was carried out in this study using SEM analysis of FIB-milled samples (Fig. 1c and Fig. 2a and 2b). As illustrated in these figures, both

aluminium and zirconium elements are uniformly distributed within the organo-silicon polymer matrix. A similar homogeneous distribution was observed in Al₂O₃ + polymer and ZrO₂ + polymer coatings, as shown in Fig. 2a and 2b. Based on the organo-silicon chemistry, we propose the following sequential reactions to explain the formation of this uniform dispersion of nano- and micro-powder within the polymer matrix. Initially, silanol-terminated PDMS and OTMS are separately mixed with ethanol and stirred vigorously for 30 min, with the quantity of OTMS (silane molecule) being four times that of the PDMS molecules. During this process, PDMS forms a highly cross-linked network of siloxane bonds ([-Si-O-Si-]) by reacting specifically with the methoxy groups [((OCH₃)₃-Si-)] of OTMS. This cross-linked network forms the backbone of the polymer matrix. The reaction simultaneously releases methanol molecules into the polymer mixture [44]. The purity of ethanol used during mixing plays a critical role in the subsequent reactions. If ethanol contains water molecules, hydrolysis of the remaining OTMS molecules can occur, leading to irreversible polymerization into a siloxane polymer [45]. This process further enhances the structural integrity and uniformity of the polymer matrix.

The primary content of OTMS remains intact in its pristine form, integrated within the PDMS-linked siloxane polymeric network. Incorporating nano- and micro-powders sequentially into the polymeric

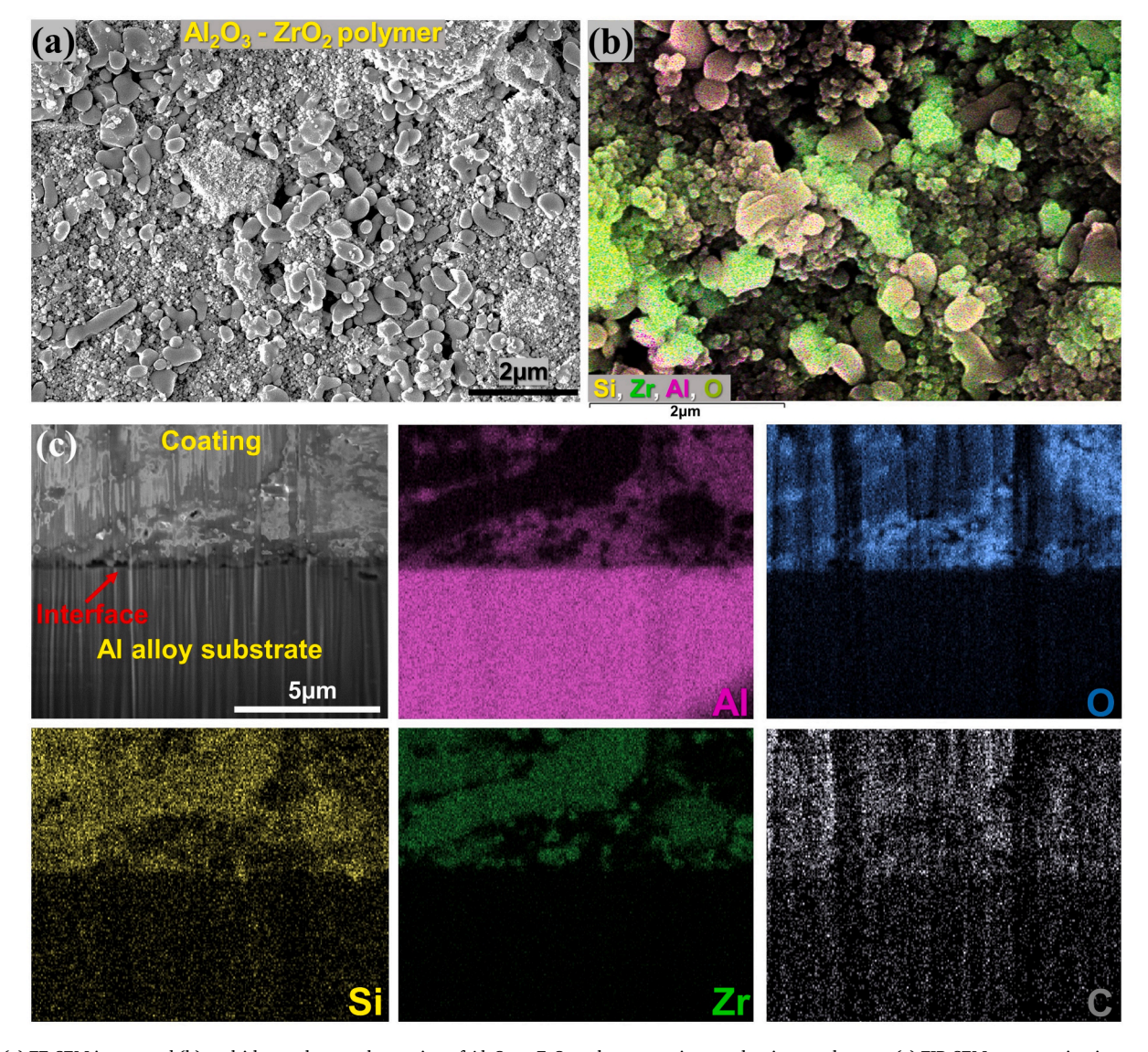


Fig. 1. (a) FE-SEM image and (b) multi-layer elemental mapping of Al₂O₃ – ZrO₂ polymer coating on aluminum substrate, (c) FIB-SEM cross-section image of Al₂O₃ – ZrO₂ polymer coating on aluminum substrate and corresponding elemental map.

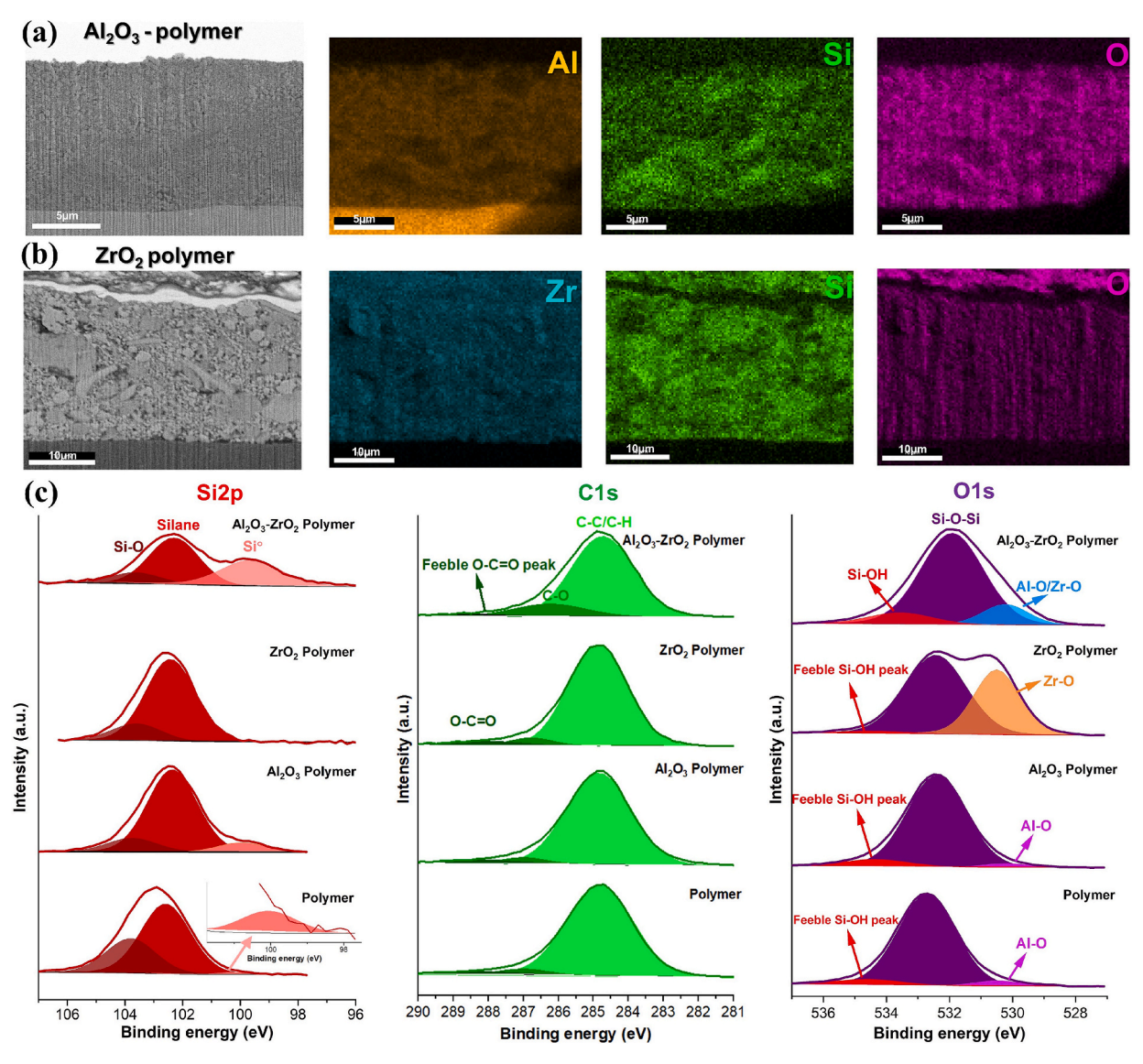


Fig. 2. FIB-SEM cross-section image of (a) Al₂O₃ and (b) ZrO₂-polymer coating on aluminum substrate and corresponding elemental map, (c) High-resolution XPS spectra of the Si 2p, C 1 s, and O 1 s energy regions on three diverse applied coatings including polymer (PDMS + Silane), Al₂O₃-polymer, ZrO₂ – polymer, and Al₂O₃ – ZrO₂ polymer coatings.

matrix results in coatings with varied chemical compositions. The surface moieties of these coatings were analyzed using XPS, as shown in Fig. 2c. When the polymeric mixture is coated on an aluminum alloy, the organosilicon compounds interact with the oxide layer on the aluminum surface, forming an Al-O-Si network, which aligns with observations from recent studies [46]. This interaction is evident in the highresolution XPS spectra. Peak fitting of the Si2p spectrum reveals a weak peak at 99.9 eV, corresponding to Si-OH bonding. The dominant peak at 102.6 eV is attributed to the silane-polymeric network, while the peak at 103.8 eV corresponds to silica particles. These findings are corroborated by analysis of the O1s spectrum, where minor peaks at 530.47 eV and 534.0 eV are associated with Al-O and Si-OH bonds, respectively, and the major peak at 532.6 eV corresponds to Si-O-Si bonds [47]. Similarly, in the C1s spectrum of the polymeric coating, a peak at 284.8 eV indicates C-C bonding, mainly arising from adventitious carbon contamination during the XPS analysis. Interestingly, when the polymeric mixture is combined with Al_2O_3 or $Al_2O_3 + ZrO_2$ powders, a significant presence of silicon particles is observed on the coating surface. This is indicated by the 99.5 eV peaks in the fitted Si2p spectrum, alongside an enhancement in the intensity of silica particle peaks. Notably, the presence of silicon particles is crucial for achieving

superhydrophobicity. In contrast, their absence in coatings without ${\rm Al_2O_3}$ nano- and micro-powders results in diminished hydrophobic properties. While ${\rm ZrO_2}$ particles form a Zr–O–Si network within the polymer matrix [45], they do not facilitate the generation of silicon particles. This explains the lower hydrophobicity observed in coatings containing only ${\rm ZrO_2}$ compared to those formulated with ${\rm Al_2O_3} + {\rm ZrO_2} + {\rm polymeric}$ mixtures.

3.2. Topography and electrical surface potential

Ceramic oxide nanoparticles, such as Al_2O_3 , ZrO_2 , and hybrid Al_2O_3 - ZrO_2 , exhibit diverse shapes, chemical compositions, and electrical properties, which substantially influence the surface roughness, morphology, and electrical surface potential/charge distribution of ceramic-polymer composite coatings. To investigate these surface properties, the topography, amplitude, and electrical surface potential/charge distribution of three distinct coatings were analyzed, as illustrated in Fig. 3. Analysis of the topography and amplitude maps (Fig. 3a1-a2, 3b1-b2, and 3c1-c2) reveals a heterogeneous distribution of nanoparticles, ranging from 40 nm to 300 nm in size. The corresponding topography histogram (Fig. 3e) shows that the Al_2O_3 -polymer

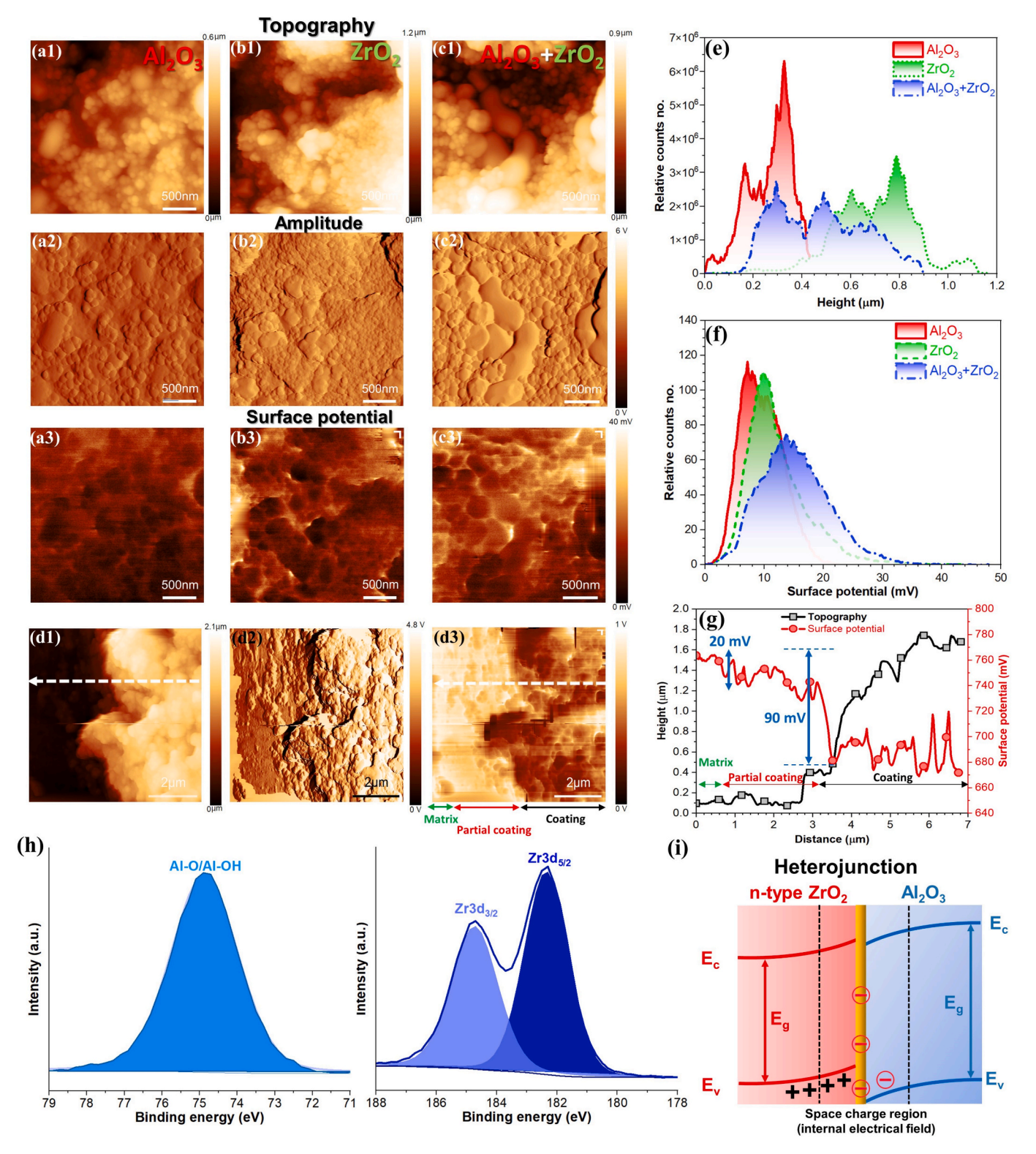


Fig. 3. Topography, amplitude, and surface potential maps of (a1-3) Al_2O_3 -polymer, (b1-3) ZrO_2 -polymer, and (c1-3) Al_2O_3 - ZrO_2 polymer, (d1) Topography, (d2) amplitude, and (d3) surface potential maps of the un-coated aluminum substrate (matrix) and Al_2O_3 - ZrO_2 polymer coating, (e) topography and (f) surface potential histogram distribution of all three different applied coatings in (a, b, and c), (g) Topography and surface potential line profiles in (d1) and (d3), (h) high-resolution XPS spectra of the Al 2p and Zr 3d energy regions on Al_2O_3 - ZrO_2 polymer coating, (i) schematic representation of heterojunction mechanism during the interactions between Al_2O_3 and ZrO_2 oxides and formation of the internal electric field.

coating exhibits the lowest mean surface roughness of 293 \pm 167 nm, while the ZrO₂-polymer coating has the highest mean value of 716 \pm 297 nm. The hybrid Al₂O₃-ZrO₂ –polymer coating demonstrates an intermediate roughness value of 474 \pm 331 nm. These findings underscore

significant differences in surface roughness and morphological distribution across the coatings. Electrical surface potential/charge maps of these composite coatings reveal a pseudo-homogeneous distribution of surface potential (Fig. 3a3, 3b3, and 3c3). As shown in the histogram

curves in Fig. 3f, the mean surface potential values progressively increase from Al_2O_3 to ZrO_2 and further to the hybrid Al_2O_3 - ZrO_2 coating, with respective values of 9.1 mV, 10.5 mV, and 14.4 mV. The increased surface potential/charge distribution in the hybrid Al_2O_3 - ZrO_2 coating is attributed to the intrinsic physicochemical properties of the individual ceramic oxides and the heterojunction effect arising from their combination (Fig. 3i) [48].

The high-resolution XPS analysis of the Al $_2$ O $_3$ -ZrO $_2$ mixed oxide (Fig. 3h) reveals a single Al 2p peak at a binding energy of 74.75 eV, which is attributed to γ - Al $_2$ O $_3$ /Al(OH) $_3$ [48–50]. The Zr 3d surface spectrum is deconvoluted into spin–orbit doublets, corresponding to Zr 3d $_5$ / $_2$ and Zr 3d $_3$ / $_2$ at binding energies of 182.33 eV and 184.7 eV, respectively. The higher binding energy of the Zr 3d $_5$ / $_2$ peak is characteristic of the Zr⁴⁺ oxidation state in ZrO $_2$ [48].

Fig. S5 presents the FTIR spectra of the Al_2O_3 -Zr O_2 coating. The absorption bands at 950 cm $^{-1}$ and 800 cm $^{-1}$ correspond to Si–O stretching and Si–OH deformation vibrations [51], respectively, indicating the presence of silanol groups. Peaks observed at 1100 cm^{-1} and 470 cm $^{-1}$ are attributed to the asymmetric and symmetric stretching modes of Si–O–Si bonds [52] within the siloxane network. A distinct band at 1262 cm^{-1} is associated with deformation vibrations of the CH₃ group bonded to silicon [53], confirming the presence of polydimethylsiloxane (PDMS).

Additionally, two minor peaks at 2930 cm⁻¹ and 2840 cm⁻¹ are

assigned to the antisymmetric and symmetric stretching vibrations of the $-\text{CH}_2$ group, characteristic of silane. These features suggest the formation of hydrocarbon chain entanglements resulting from monomer polymerization on the surface, as well as potential electron-withdrawing effects from adjacent carbonyl groups. The peak at 1450 cm $^{-1}$ is ascribed to Si–CH $_2$ bending vibrations, further indicating the presence of silane. Overall, the detection of these characteristic bands of silane and PDMS confirms the successful formation of a self-assembled silane/ PDMS coating on the aluminum substrate surface.

When these oxide nanoparticles interact physicochemically, an internal electric field is generated, as illustrated in Fig. 3i. This arises from band bending at the $\mathrm{Al}_2\mathrm{O}_3$ and ZrO_2 oxide energy levels, coupled with the formation of a space charge region [49]. The SKPFM results in Fig. 3a3, 3b3, and 3c3 highlight a more pronounced heterojunction effect in the mixed $\mathrm{Al}_2\mathrm{O}_3$ - ZrO_2 coating compared to the individual $\mathrm{Al}_2\mathrm{O}_3$ and ZrO_2 coatings. This is evidenced by a higher potential and charge distribution at the nanoparticle interfaces and their immediate surroundings [50]. In contrast, Fig. 3d displays the topography, amplitude, and surface potential/charge maps across three distinct regions: the Al matrix (a small region), a partially coated area (with a thinner coating), and a heavily coated area. The surface potential/charge map and corresponding line profiles in Fig. 3g show that the surface potential in the Al matrix is approximately 20 mV higher than in the partially coated region, while the difference between the Al matrix and the thickly

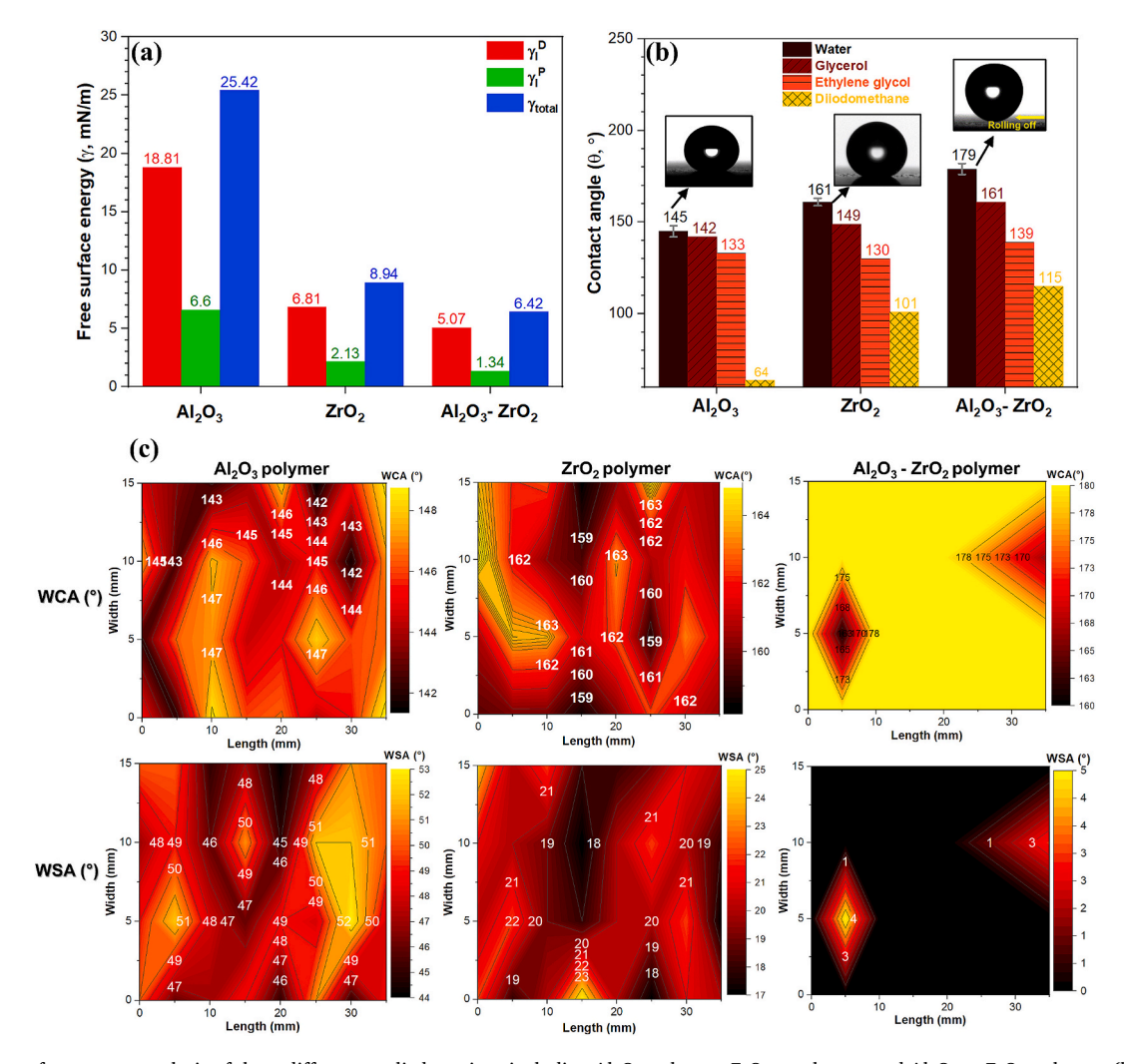


Fig. 4. (a) Free surface energy analysis of three different applied coatings including Al_2O_3 -polymer, ZrO_2 -polymer, and Al_2O_3 - ZrO_2 polymer, (b) contact angle analyses based on various droplets including water, glycerol, ethylene glycol, diiodomethane regions on the surface of three different applied coatings including Al_2O_3 -polymer, ZrO_2 -polymer, and ZrO_3 -polymer, ZrO_2 -polymer, and ZrO_3 -polymer, ZrO_3 -polymer, ZrO_3 -polymer, and ZrO_3 -polymer coatings in multiple random regions.

coated area is around 90 mV (Surface potential of an aluminum substrate and polymer coating alone is presented in Fig. S6). This reduction in surface potential and charge accumulation in the mixed $\rm Al_2O_3\text{-}ZrO_2$ coating indicates a lower tendency for electrochemical activity and charge transfer at the solid/liquid interface within these regions.

3.3. Water contact angle and free surface energy

The contact angle and free surface energy of various ceramicpolymer coatings are analyzed, with the results presented in Fig. 4a and 4b. Among the three coatings studied Al₂O₃-polymer, ZrO₂-polymer, and Al₂O₃ -ZrO₂ polymer, a decreasing trend is observed in all free surface energy components, including the dispersive (γ_1^D) , polar (γ_1^P) , and total surface energy (γ^{total}), following the order: Al₂O₃-polymer > ZrO₂polymer > Al₂O₃ -ZrO₂ polymer. Interestingly, this trend is inversely related to the contact angle, which decreases in the same order for the various liquids (Fig. S7b): Al₂O₃-polymer < ZrO₂-polymer < Al₂O₃ -ZrO₂. Fig. 4c demonstrates the graduated color bar representing the WCA values determined through digital image analysis software. The distribution of WCAs was relatively homogeneous across the surface. Except for Al₂O₃-polymer coating, all WCA values exceeded 150°, suggesting that the proposed surface treatment method is effective in generating hierarchical superhydrophobic surfaces. Specifically, the dip-coating process may lead to the thickening of the silane layer at the specimen bottom edge, which results in a reduction of surface roughness as the silane deposits in the valleys, thereby decreasing the local WCA. In contrast, the upper edge, likely featuring a more uniform silane coating, displays a higher WCA. This variation accounts for the presence of localized low- or high-contact-angle regions. Fig. S7a presents overall optical images of the Al₂O₃ -ZrO₂ polymer coating immersed in tea media for the self-cleaning test, along with single droplet images of various liquids on the coating, indicating excellent self-cleaning performance.

Upon examining Fig. 4c, it is observed that the difference between the minimum and maximum contact angles during the wettability map analysis was approximately 10°. However, the average WCA was 160.0°, with a standard deviation of 2.4°. While these results indicate some dispersion in the data, surface homogeneity remains acceptable, especially considering the large analysis area (720 mm²). Except for Al₂O₃polymer coating, all samples exhibited WCA above the 150° threshold; only the Al₂O₃ –ZrO₂ polymer samples showed a low water sliding angle (WSA $< 5^{\circ}$), suggesting a transition from the Wenzel to the Cassie-Baxter regime [16]. In this regime, the combined effects of high roughness and hydrophobicity result in air pockets being trapped at the droplet-substrate interface. This enhances the hydrophobic behavior, as predicted by the Cassie-Baxter model, yielding a significantly high contact angle. Additionally, the entrapped air reduces the contact area between the liquid droplet and the substrate, facilitating water rolling at low tilting angles [18]. In contrast, this phenomenon was not observed for the Al₂O₃-polymer samples, where the rolling angle exceeded 90°. Despite the addition of a hydrophobic silane layer, the surface remained in the Wenzel state. In the Wenzel state, the water droplet penetrates the surface grooves, with the liquid/air/solid contact line being continuous and stable. This mode is often referred to as homogeneous wetting. According to existing literature [54-56], adhesion forces in the Wenzel state are related to van der Waals forces and the negative pressures caused by the air trapped within the surface. When a droplet is placed on a superhydrophobic surface, these negative pressures are negligible. Upon tilting the surface, the air-water contact line shifts from concave to convex, causing the trapped air volume to increase [57,58]. This expansion of the sealed air amplifies the negative pressure, thereby enhancing liquid adhesion. A high water contact angle (WCA) generally reflects low surface energy combined with micro/nano-scale roughness that resists wetting. In contrast, a high water sliding angle (WSA) suggests strong droplet pinning, often caused by surface defects, chemical heterogeneity, or disruptions in hierarchical structure [59,60]. For the

ZrO₂-polymer coating, this may result from non-uniform nanoscale roughness or partial transitions to the Wenzel state, where water penetrates the texture, increasing friction and hindering droplet mobility.

3.4. Dynamic droplet monitoring, vapor condensation, and anti-icing properties

To thoroughly assess the performance of the superhydrophobic surface across various water states, we conducted dynamic droplet monitoring, evaluated vapor condensation, and investigated the anti-icing behavior (ice shear stress test). These experiments offer valuable insights into the coating functionality under diverse environmental conditions. The detailed results of these analyses are presented in Fig. 5. Fig. 5a captures the dynamic behavior of a water droplet falling freely from a height of 30 mm onto the Al₂O₃-ZrO₂ ultra superhydrophobic surface, impacting the substrate with a velocity of 500 mm/s. Upon impact, the droplet momentarily assumes a nearly spherical shape before spreading outward, achieving its maximum spread diameter at 200 ms. During this phase, the droplet's potential energy is completely converted into kinetic energy. However, part of this kinetic energy is transformed into surface energy, dissipating as the droplet overcomes the surface's sliding friction and adhesion forces [60,61]. Due to the droplet's vertical inertia exceeding the combined forces of gravity and surface tension, it rebounds fully upward at 300 ms, performing an elastic bounce before rolling off the coated surface without leaving any trace of water (Movie S3). These observations emphasize the remarkable wetting resistance of the Al₂O₃-ZrO₂ ultra superhydrophobic surface. Its superior hydrophobicity and low adhesion properties drastically reduce both the contact time and area of the droplet, allowing it to either bounce off or roll away rapidly.

Thermal imaging monitored the ice melting process was performed on both an aluminum substrate and an Al2O3-ZrO2 ultrasuperhydrophobic surface (Fig. 5b). These samples were cooled in a fridge to $-20~^{\circ}\text{C}$ for 48 h, and then exposed to ambient temperature $(\sim 19 \, ^{\circ}\text{C})$. The temperature of the uncoated surface gradually increased, reaching ambient temperature after 480 s. In contrast, the Al₂O₃-ZrO₂ ultra-superhydrophobic surface remained significantly cooler than the ambient temperature even after 600 s. The delayed temperature change observed during the deicing process on ultra superhydrophobic surfaces, compared to hydrophilic surfaces, can be attributed to differences in heat transfer mechanisms, ice formation, and the influence of the air film on the surface [62]. Superhydrophobic surfaces exhibit minimal contact between water or ice and the substrate due to their highly repellent properties. This leads to the formation of a stable air film between the ice and the surface, further reducing thermal conduction. As air is a poor conductor of heat, it acts as an insulating barrier that slows the transfer of heat from the surrounding environment to the coating, thereby delaying the melting process. In contrast, on hydrophilic surfaces, water spreads more readily across the surface, increasing the contact area and facilitating efficient heat transfer, which accelerates the melting of ice [63]. As a result, the superhydrophobic surface experiences a slower rise in temperature, indicating minimal ice formation on it. This behavior highlights the role of surface energy, the presence of the air film, and the heat transfer properties on ice adhesion and melting efficiency.

Vapor condensation was observed on both an aluminum substrate and an Al_2O_3 -ZrO $_2$ ultra-superhydrophobic coating during exposure to hot vapor at 70 °C (Fig. 5C). On the aluminum substrate (19 °C), a thin, uniform film of water rapidly covered the entire surface within 120 s, demonstrating the material's strong condensation-promoting properties. The vapor efficiently condensed into liquid water, spreading evenly across the substrate. In contrast, Al_2O_3 -ZrO $_2$ ultra-superhydrophobic coating showed no condensation during the same time frame. After 1500 s, the water film on the uncoated aluminum had thickened, indicating ongoing condensation and accumulation. On the Al_2O_3 -ZrO $_2$ ultra-superhydrophobic coating, however, water droplets only appeared at the lower region, where the contact angle was reduced due to a

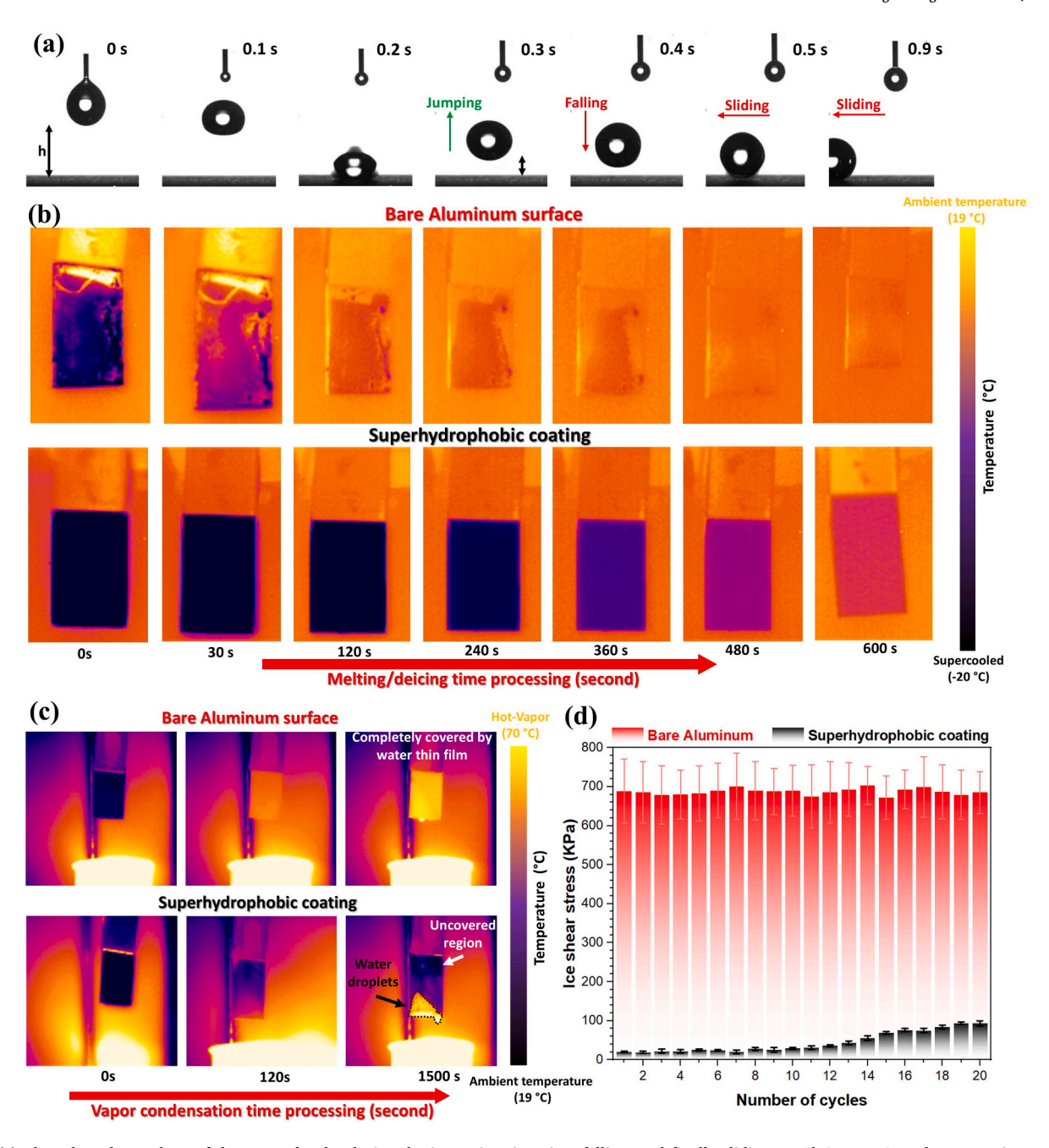


Fig. 5. (a) The selected snapshots of the water droplet during the impacting, jumping, falling, and finally sliding on $Al_2O_3 - ZrO_2$ polymer coating as an ultrasuperhydrophobic surface, (b) the thermal snapshot monitoring of the ice melting process on both aluminium substrate and $Al_2O_3 - ZrO_2$ polymer coating as an ultra-superhydrophobic surface extracted from supercooled media ($-20~^{\circ}C$) then exposed to ambient temperature, (c) vapor condensation monitoring of both aluminium substrate and $Al_2O_3 - ZrO_2$ polymer coating as an ultra-superhydrophobic surface during exposure to hot vapor media ($70~^{\circ}C$), (d) ice shear stress versus the number of cycles curves of both aluminium substrate and $Al_2O_3 - ZrO_2$ polymer coating as an ultra-superhydrophobic surface.

doping process, as shown in the wetting maps in Fig. 4c. These droplets swiftly slid off, reflecting the low adhesion and water-repellent behavior characteristic of superhydrophobic surfaces.

Fig. 5d compares the ice adhesion forces of the Al_2O_3 - ZrO_2 ultrasuperhydrophobic coating and an uncoated control. The ultrasuperhydrophobic surface demonstrated a significantly lower ice adhesion, primarily due to the Cassie-Baxter state, in which a trapped air layer minimizes direct contact between the ice and the surface. This results in partial wetting, with only a few isolated contact points between the ice and the surface, substantially reducing overall adhesion. In some cases, the reduction in contact is so pronounced that the ice shows near-complete detachment from the surface, minimizing adhesion to a

remarkable extent. Specifically, the ice shear stress on the $\rm Al_2O_3\text{-}ZrO_2$ ultra-superhydrophobic surface was only 20 kPa, compared to approximately 700 kPa for the uncoated surface. This substantial difference underscores the effectiveness of the $\rm Al_2O_3\text{-}ZrO_2$ ultra-superhydrophobic coating in reducing ice attachment. For the uncoated surface, the ice adhesion force remained stable at around 700 kPa even after 20 detachment cycles, indicating a strong resistance to changes in adhesion strength during repeated freeze—thaw cycles. In contrast, the $\rm Al_2O_3\text{-}ZrO_2$ ultra-superhydrophobic coating imagined a slight increase in ice adhesion to 40 kPa after 14 cycles, though it remained significantly lower than that of the uncoated surface. By the end of the 20 cycles, the $\rm Al_2O_3\text{-}ZrO_2$ ultra-superhydrophobic coating still exhibited an ice adhesion

force below 100 kPa, demonstrating its sustained performance and stability under prolonged icing conditions. This behavior aligns with the broader literature on passive icephobic coatings, where minimizing ice adhesion strength is crucial for practical applications, with values below 100 kPa considered ideal for efficient ice removal with minimal external loading [64,65]. Furthermore, these ice detachment experiments also served as an indirect evaluation of the coating's durability and scratch resistance. Despite repeated detachment cycles, the coated sample maintained its icephobic performance without observable damage. This indicates that the $\rm Al_2O_3\text{-}ZrO_2$ ultra-superhydrophobic coating is not only highly effective in reducing ice adhesion but also durable under repeated mechanical stresses [64,66,67].

The ceramic-polymer hybrid coating developed in this study exhibits exceptional multifunctional performance, particularly in superhydrophobicity, icephobicity, and long-term durability. The Al₂O₃-ZrO₂ coating achieved an impressive water contact angle (WCA) of 180° and an ultralow ice shear stress of just 20 kPa, outperforming many advanced coatings reported in recent literature (see Table 2). For comparison, Polytetrafluoroethylene (PTFE)-fluorinated epoxy coatings demonstrate a WCA of 156.8° with an ice shear stress of 51 kPa [68], while 1H,1H,2H,2H-perfluorooctyltriethoxysilane (FOTS)-coated steel (WCA: 151°) exhibits a significantly higher ice adhesion strength of 207 kPa [69]. Other composite systems, including multi-walled carbon nanotubes (MWCNTs)- cetyltrimethylsiloxane (HDTMS)-epoxy (WCA: kPa) [70], metal-organic frameworks (MOF)-MxNS-1H,1H,2H,2H-perfluorodecyltrimethoxysilane (PFTS) (WCA: 159°, 55 kPa) [71], and octadecyltrichlorosilane (OTS)-MOF-Cu (WCA: 155.8°, 45.7 kPa) [72], also fall short in both water repellency and icephobic performance. In contrast, our composite coating not only achieves ultra-superhydrophobicity but also maintains excellent antiicing, anti-vapor condensation, and corrosion-resistant properties, positioning it as a highly promising solution for use in extreme and demanding operational environments.

Additionally, to assess the mechanical durability of the superhydrophobic coating, a controlled scratch test was conducted using a cut-off knife with a blade thickness of 0.7 mm, as shown in Fig. S7c. The surface was deliberately scratched to simulate mechanical damage, after which water droplets were applied to the affected area. Remarkably, the coating maintained its superhydrophobic characteristics even after damage, as evidenced by the formation of nearly spherical water droplets and a static contact angle exceeding 150°. These results demonstrate that the coating possesses excellent resistance to mechanical abrasion while preserving its water-repellent properties.

3.5. Short and long-term corrosion protective performance

To evaluate the chemical stability of Al₂O₃-ZrO₂ ultrasuperhydrophobic coating and its corrosion protection of aluminum substrates, both short- and long-term corrosion analyses were performed alongside contact angle measurements. Fig. 6a presents the potentiodynamic polarization curves for the as-received aluminum substrate and

Table 2Comparison of the water contact angle (WCA) and ice adhesion strength of various advanced coatings with the coating developed in this study.

Materials	WCA (°)	Ice adhesion strength (kPa)	References
PTFE, fluorinated epoxy	156.8°	51	[68]
FOTS, Steel	151	207	[69]
MWCNTs, HDTMS, Epoxy	156	105.2	[70]
MOF-MXNS, PFTS	159	55	[71]
OTS, MOF, Cu	155.8	45.7	[72]
PDMS@Silane, ZrO_2 , Al_2O_3	180	20	Our developed coating

the Al₂O₃-ZrO₂ ultra-superhydrophobic coating, characterized by varying WCA in a 3.5 wt% NaCl solution. Key electrochemical parameters, including corrosion current density (i_{corr}) and corrosion potential (E_{corr}), were determined using the Tafel extrapolation method and are shown in Fig. 6c and 6d to quantify corrosion protection performance. A substantial reduction in i_{corr} (4.1nA.cm⁻²) and a significant increase in E_{corr} (47 mV vs. Ag/AgCl) highlight the enhanced corrosion resistance of the coated sample. The results indicate a positive shift in the corrosion potential of the aluminum substrate with the application of Al₂O₃-ZrO₂ ultra-superhydrophobic coating. This improvement is attributed to the enhanced water repellency provided by the hierarchical rough structures of the coating, which trap air and form an insulating "cushion." This air cushion acts as a barrier, reducing the diffusion of aggressive electrolytes to the metal surface. Additionally, the self-assembled silane layer reinforces this barrier, creating a dual protective effect that significantly enhances corrosion resistance. In contrast, the untreated substrate permits rapid interaction and penetration of corrosive ions (e. g., Cl –), leading to reduced corrosion resistance. The synergistic effect of surface texturing (air entrapment within micro/nanostructures) and silanization (energy barrier for water penetration [73]) is crucial for achieving exceptional corrosion protection. These findings align with previous studies that reported improved corrosion protective performance in superhydrophobic aluminum alloy surfaces compared to untreated alloys [22], while another study observed similar enhancements for aluminum in sterile seawater [21]. Moreover, the SEM images of the Al₂O₃-ZrO₂ ultra-superhydrophobic coating (Fig. 6e and 6f), taken after the potentiodynamic polarization test, show no signs of degradation, breakdown, or detachment. This indicates excellent chemical stability and outstanding corrosion resistance of Al₂O₃-ZrO₂ ultrasuperhydrophobic coating in 3.5 wt% NaCl aggressive environment.

Fig. 6b presents the open circuit potential (OCP) values in 3.5 % NaCl for both the aluminum alloy and Al₂O₃-ZrO₂ ultra-superhydrophobic coating. The WCA data indicates that silane treatment and hierarchical micro/nanostructures effectively keep the chemical stability and trap air in surface valleys, preserving ultra-superhydrophobic properties for up to 210 days in a 3.5 % NaCl solution. After approx. 50 days of immersion, the OCP value reflects a corrosion potential of 40 mV vs. Ag/ AgCl, indicating excellent chemical stability and corrosion protection performance. After this period, the OCP values exhibit a gradual decrease until the coating stabilizes at an average of -120 mV vs. Ag/ AgCl by 285 days. Throughout the exposure period, the WCA values remain stable, with only minor changes, reaching approximately 174°, demonstrating the robust chemical stability of the Al₂O₃-ZrO₂ ultrasuperhydrophobic coating. This stability is attributed to the strong interfacial bonding and the synergistic effects of the silane treatment (especially siloxane bonds (-Si-O-Si-)) with the Al₂O₃-ZrO₂ components. In conclusion, the proposed mixed Al₂O₃-ZrO₂ polymer coating significantly enhances the water repellency, chemical stability, and corrosion shield of AA6082-T6, showcasing its potential for advanced anti-icing, anti-vapor condensation, scratching resistance, and corrosion protection in industrial applications.

4. Conclusion

In this study, we successfully developed a mechanically robust, cost-effective, and scalable Al₂O₃-ZrO₂ ultra-superhydrophobic coating with a hierarchical micro-nano structure, applicable to a wide range of materials, ranging from aluminum to concrete. This surface was fabricated through a simple, single-step process, enabling efficient production. We evaluate the individual and synergistic effects of alumina (Al₂O₃) and zirconia (ZrO₂) on superhydrophobicity, demonstrating outstanding enhanced overall surface physical and chemical properties. The Al₂O₃-ZrO₂ ultra-superhydrophobic coating exhibits exceptional multifunctionality, including superhydrophobic, anti-icing, anti-corrosion, anti-vapor condensation, scratching resistance, and self-cleaning properties. It retains its non-wetting characteristics even when exposed to

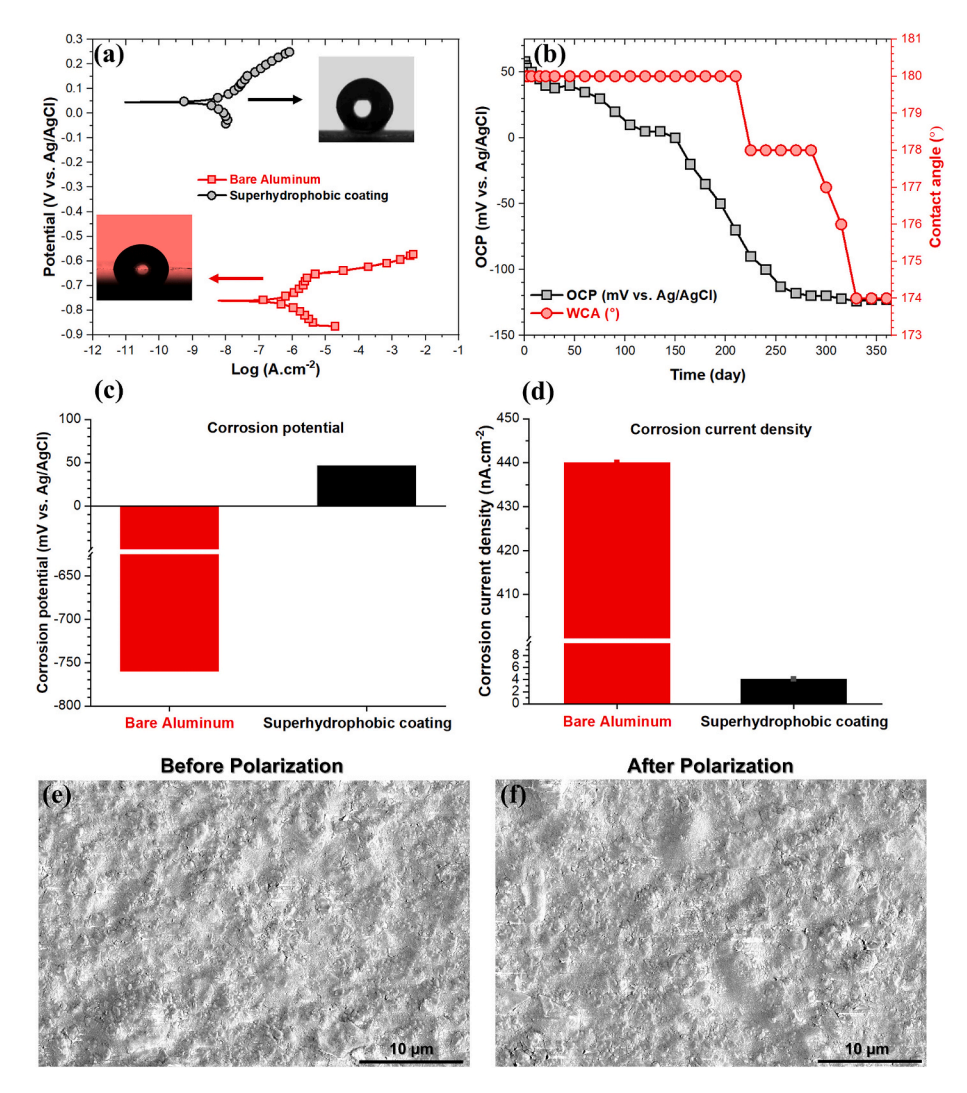


Fig. 6. (a) Potentiodynamic polarization (PDP) curves of both aluminum substrate and $Al_2O_3 - ZrO_2$ polymer coating as an ultra-superhydrophobic surface during exposure to NaCl 3.5% wt. NaCl media, inserted contact angle images analyzed after PDP measurement, (b) The long-term open circuit potential (OCP) and water contact angle (WCA) monitoring of $Al_2O_3 - ZrO_2$ polymer coating as an ultra-superhydrophobic surface during exposure to NaCl 3.5% wt. NaCl media, (c) Corrosion potential, and (d) corrosion current density values extracted from curves in (a), (e,f) SEM images of the Al_2O_3 -ZrO₂ polymer coating as an ultra-superhydrophobic after PDP test.

various liquids, highlighting its durability in diverse environments. The surface morphology and chemical composition analyses confirmed the critical role of hierarchical structures in influencing wettability and other properties. Overall, this innovative ${\rm Al_2O_3\text{-}ZrO_2}$ polymer composite coating, as an ultra-superhydrophobic coating, not only addresses current limitations in superhydrophobic surface technology but also paves the way for large-scale industrial applications. Its simplified fabrication process, combined with enhanced mechanical and chemical stability, positions it as a promising solution for industries requiring advanced surface functionalities, such as aerospace, marine, construction, and energy sectors.

CRediT authorship contribution statement

Amani Khaskhoussi: Writing – review & editing, Writing – original draft, Methodology, Investigation, Formal analysis, Data curation, Conceptualization, Visualization. Ehsan Rahimi: Writing – review & editing, Methodology, Investigation, Formal analysis, Data curation, Conceptualization, Visualization. Luigi Calabrese: Writing – review & editing, Methodology, Investigation. Arjan Cornet: Writing – review & editing, Investigation, Formal analysis, Data curation. Prasaanth Ravi Anusuyadevi: Writing – review & editing, Methodology, Investigation,

Formal analysis, Data curation. **Prasad Gonugunta:** Formal analysis, Data curation. **Arjan Mol:** Writing – review & editing, Visualization, Validation, Supervision, Resources, Project administration, Funding acquisition. **Edoardo Proverbio:** Writing – review & editing, Visualization, Validation, Supervision, Resources, Project administration, Funding acquisition.

Declaration of competing interest

The authors declare that they have no known competing financial interests or personal relationships that could have appeared to influence the work reported in this paper.

Acknowledgments

The authors acknowledge the University of Messina and Delft University of Technology (TUDelft) for financial support and for providing experimental facilities.

Appendix A. Supplementary data

Supplementary data to this article can be found online at https://doi.

org/10.1016/j.cej.2025.163767.

Data availability

Data will be made available on request.

References

- [1] R. Carriveau, A. Edrisy, P. Cadieux, R. Mailloux, Ice adhesion issues in renewable energy infrastructure, J. Adhes. Sci. Technol. 26 (4–5) (2012) 447–461.
- [2] N. Dalili, A. Edrisy, R. Carriveau, A review of surface engineering issues critical to wind turbine performance, Renew. Sustain. Energy Rev. 13 (2) (2009) 428–438.
- [3] T. Bretterklieber, M. Neumayer, M. Flatscher, A. Becke, G. Brasseur, Model based monitoring of ice accretion on overhead power lines, 2016 IEEE International Instrumentation and Measurement Technology Conference Proceedings, IEEE, 2016, pp. 1-6..
- [4] S. Rastayesh, L. Long, J. Dalsgaard Sørensen, S. Thöns, Risk assessment and value of action analysis for icing conditions of wind turbines close to highways, Energies 12 (14) (2019) 2653.
- [5] L. Matejicka, C.T. Georgakis, A review of ice and snow risk mitigation and control measures for bridge cables, Cold Reg. Sci. Technol. 193 (2022) 103429.
- [6] W. He, W. Ma, H. Ye, H. Wu, V.T. Tran, X. Chen, Y. Huang, J. An, Stretchable superhydrophobic laser-induced graphene heaters with high heating rate for robust passive anti-icing and rapid active de-icing, Chem. Eng. J. 507 (2025) 160424.
- [7] S. Liu, Z. Zhu, Q. Zheng, K. Wang, F. Zhou, Q. Yang, X. Wang, L. Ye, Y. Chen, H. Liu, H. Li, Waxberry-liked micro-nanostructured, superhydrophobic surfaces with enhanced photothermal de-icing and passive anti-icing properties, Chem. Eng. J. 503 (2025) 158358.
- [8] Z. Zehui, W. Zelinlan, L. Guang, C. Dengke, Z. Kaiteng, Z. Yantong, C. Jichen, S. Shize, L. Xiaolin, C. Huawei, Liquid-like slippery surface with passive-multi active strategy integration for anti-icing/de-icing, Chem. Eng. J. 474 (2023) 145541.
- [9] P.-O.-A. Borrebæk, B.P. Jelle, Z. Zhang, Avoiding snow and ice accretion on building integrated photovoltaics-challenges, strategies, and opportunities, Sol. Energy Mater. Sol. Cells 206 (2020) 110306.
- [10] S.R. Corsi, S.W. Geis, J.E. Loyo-Rosales, C.P. Rice, R.J. Sheesley, G.G. Failey, D. A. Cancilla, Characterization of aircraft deicer and anti-icer components and toxicity in airport snowbanks and snowmelt runoff, Environ. Sci. Tech. 40 (10) (2006) 3195–3202.
- [11] Y. Liu, Y. Wu, S. Liu, F. Zhou, Material strategies for ice accretion prevention and easy removal, ACS Mater. Lett. 4 (2) (2021) 246–262.
- [12] A. Dhyani, W. Choi, K. Golovin, A. Tuteja, Surface design strategies for mitigating ice and snow accretion, Matter 5 (5) (2022) 1423–1454.
- [13] X.-M. Li, D. Reinhoudt, M. Crego-Calama, What do we need for a superhydrophobic surface? a review on the recent progress in the preparation of superhydrophobic Surfaces, Chem. Soc. Rev. 36 (8) (2007) 1350–1368.
- [14] J. Cheng, Y. Zhu, F. Zhan, L. Wang, Lotus leaf-inspired thermal insulation and antiicing topography, RSC Adv. 14 (26) (2024) 18798–18806.
- [15] H.Y. Erbil, C.E. Cansoy, Range of applicability of the Wenzel and Cassie—Baxter equations for superhydrophobic surfaces, Langmuir 25 (24) (2009) 14135–14145.
- [16] D. Murakami, H. Jinnai, A. Takahara, Wetting transition from the Cassie–Baxter state to the Wenzel state on textured polymer surfaces, Langmuir 30 (8) (2014) 2061–2067.
- [17] E. Rahimi, A. Rafsanjani-Abbasi, A. Davoodi, A. Kiani-Rashid, Shape evolution of water and saline droplets during icing/melting cycles on superhydrophobic surface. Surf. Coat. Technol. 333 (2018) 201–209.
- surface, Surf. Coat. Technol. 333 (2018) 201–209.

 [18] J.T. Simpson, S.R. Hunter, T. Aytug, Superhydrophobic materials and coatings: a review, Rep. Prog. Phys. 78 (8) (2015) 086501.
- [19] C. Zhou, Z. Chen, H. Yang, K. Hou, X. Zeng, Y. Zheng, J. Cheng, Nature-inspired strategy toward superhydrophobic fabrics for versatile oil/water separation, ACS Appl. Mater. Interfaces 9 (10) (2017) 9184–9194.
- [20] E. Vazirinasab, R. Jafari, G. Momen, Application of superhydrophobic coatings as a corrosion barrier: a review, Surf. Coat. Technol. 341 (2018) 40–56.
- [21] M. Ran, W. Zheng, H. Wang, Fabrication of superhydrophobic surfaces for corrosion protection: a review, Mater. Sci. Technol. 35 (3) (2019) 313–326.
- [22] S. Zheng, C. Li, Q. Fu, W. Hu, T. Xiang, Q. Wang, M. Du, X. Liu, Z. Chen, Development of stable superhydrophobic coatings on aluminum surface for corrosion-resistant, self-cleaning, and anti-icing applications, Mater. Des. 93 (2016) 261–270.
- [23] L. Feng, Z. Yan, X. Qiang, Y. Liu, Y. Wang, Facile formation of superhydrophobic aluminum alloy surface and corrosion-resistant behavior, Appl. Phys. A 122 (2016) 1–14.
- [24] M. Ruan, W. Li, B. Wang, Q. Luo, F. Ma, Z. Yu, Optimal conditions for the preparation of superhydrophobic surfaces on al substrates using a simple etching approach, Appl. Surf. Sci. 258 (18) (2012) 7031–7035.
- [25] Z. Chen, Y. Guo, S. Fang, A facial approach to fabricate superhydrophobic aluminum surface, Surface Interface Anal. 42 (1) (2010) 1–6.
- [26] Y. Shi, X. Xiao, W. Zhang, Facile fabrication of superhydrophobic surface with needle-like microflower structure on aluminum substrate, J. Coat. Technol. Res. 12 (2015) 1143–1151.
- [27] W. Dou, J. Wu, T. Gu, P. Wang, D. Zhang, Preparation of super-hydrophobic microneedle CuO surface as a barrier against marine atmospheric corrosion, Corros. Sci. 131 (2018) 156–163.

- [28] X. Li, Q. Zhang, Z. Guo, T. Shi, J. Yu, M. Tang, X. Huang, Fabrication of superhydrophobic surface with improved corrosion inhibition on 6061 aluminum alloy substrate, Appl. Surf. Sci. 342 (2015) 76–83.
- [29] A. Khaskhoussi, L. Calabrese, E. Proverbio, Anticorrosion superhydrophobic surfaces on AA6082 aluminum alloy by HF/HCl texturing and self-assembling of silane monolayer, Materials 15 (23) (2022) 8549.
- [30] A.Y. Fadeev, T.J. McCarthy, Self-assembly is not the only reaction possible between alkyltrichlorosilanes and surfaces: monomolecular and oligomeric covalently attached layers of dichloro-and trichloroalkylsilanes on silicon, Langmuir 16 (18) (2000) 7268–7274.
- [31] A. Khaskhoussi, L. Calabrese, E. Proverbio, Superhydrophobic self-assembled silane monolayers on hierarchical 6082 aluminum alloy for anti-corrosion applications, Appl. Sci. 10 (8) (2020) 2656.
- [32] G. Yang, Y. Zhang, Z. Yin, Y. Deng, Z. Li, Y. Xie, Y. Chen, C. Yang, H. Yang, Y. Luo, Z. Hong, M. Xue, Robust mussel-inspired LBL carbon nanotube-based superhydrophobic polyurethane sponge for efficient oil—water separation utilizing photothermal effect, Fuel 381 (2025) 133353.
- [33] R. Wang, Z. Yin, G. Yang, Q. Zha, C. Xiong, Y. Xie, J. Xu, Y. Luo, Z. Hong, C. Xie, M. Xue, Highly efficient multifunctional 3D polyurethane sponge with photothermal responsiveness for efficient oil-water separation and microplastic extraction, Desalination 601 (2025) 118604.
- [34] G. Yang, Z. Yin, Q. Zha, R. Wang, Y. Xie, Y. Chen, Z. Hong, Y. Luo, M. Xue, A typha orientalis-inspired 3D Janus solar evaporator with controllable wettability for highly efficient and stable solar desalination, Desalination 595 (2025) 118318.
- [35] G. Yang, Z. Yin, Y. Deng, Z. Li, Y. Chen, W. Xiao, Z. Hong, Y. Luo, C. Xie, M. Xue, Fabrication of flexible multifunctional graphene-based composite membrane with improved hydrophobicity and thermal conductivity characters for thermal management, Colloids Surf A Physicochem Eng Asp 704 (2025) 135494.
- [36] Z. Yin, X. Chen, Z. Chen, H. Song, P. Lv, M. Xue, H. Li, Superhydrophobic photocatalytic self-cleaning nanocellulose-based strain sensor for full-range human motion monitoring, Adv. Mater. Interfaces 10 (33) (2023) 2300350.
- [37] J. Cheng, Y. Ge, B. Wang, L. Zhang, X. Hu, S. Hong, X. Liang, X. Zhang, Microstructure and tribocorrosion behavior of Al2O3/Al composite coatings: role of Al2O3 addition, J. Therm. Spray Technol. 29 (7) (2020) 1741–1751.
- [38] N.P. Patel, K.V. Chauhan, R.N. Prajapati, Anti-icing, wettability and structural characterization of Zirconia thin films, Mater. Today: Proceed., 2023.
- [39] J. Zhang, A. Kobayashi, Corrosion resistance of the Al2O3+ZrO2 thermal barrier coatings on stainless steel substrates, Vacuum 83 (1) (2008) 92–97.
- [40] S. Dong, B. Maciejewska, R. Millar, N. Grobert, 3D Electrospinning of Al2O3/ZrO2 fibrous aerogels for multipurpose thermal insulation, Adv. Compos. Hybrid Mater. 6 (5) (2023) 186.
- [41] F. Li, M. Zhao, Y. Zhan, C. Wu, Y. Zhang, X. Jiang, Z. Sun, Facile fabrication of novel superhydrophobic Al2O3/polysiloxane hybrids coatings for aluminum alloy corrosion protection, Colloids Surf A Physicochem Eng Asp 640 (2022) 128444.
- [42] M. Balordi, F. Pini, G. Santucci de Magistris, Superhydrophobic ice-phobic zinc surfaces, Surf. Interfaces 30 (2022) 101855.
- [43] L.B. Boinovich, E.V. Chulkova, K.A. Emelyanenko, A.G. Domantovsky, A. M. Emelyanenko, The mechanisms of anti-icing properties degradation for slippery liquid-infused porous surfaces under shear stresses, J. Colloid Interface Sci. 609 (2022) 260–268
- [44] M. Irfan, C.N. Lakshmi, N. Singh, Nonfluorinated, robust and anti-corrosive polydimethylsiloxane/OTMS functionalized-SiO2 superhydrophobic coating on inconel alloy, New J. Chem. 48 (25) (2024) 11201–11205.
- [45] P. Zhang, X. Yin, W. Li, L. Feng, Preparation, properties and formation mechanism of zirconium-Si hybrid high transmittance hydrophobic coating, Colloids Surf A Physicochem Eng Asp 631 (2021) 127649.
- [46] V. Rozyyev, J.G. Murphy, E. Barry, A.U. Mane, S.J. Sibener, J.W. Elam, Vapor-phase grafting of a model aminosilane compound to Al2O3, ZnO, and TiO2 surfaces prepared by atomic layer deposition, Appl. Surf. Sci. 562 (2021) 149996.
- [47] J.W. Ma, W.J. Lee, J.M. Bae, K.S. Jeong, S.H. Oh, J.H. Kim, S.H. Kim, J.H. Seo, J. P. Ahn, H. Kim, M.H. Cho, Carrier mobility enhancement of tensile strained Si and SiGe nanowires via surface defect engineering, Nano Lett. 15 (11) (2015) 7204–7210.
- [48] Z. Xu, B. Kaczer, R. Degraeve, S. De Gendt, M. Heyns, G. Groeseneken, Electrical properties of Al2 O 3/ZrO2/Al2 O 3 gate stack in p-substrate metal oxide semiconductor devices, J. Electrochem. Soc. 150 (5) (2003) G307.
- [49] A.I. Osman, J.K. Abu-Dahrieh, M. McLaren, F. Laffir, P. Nockemann, D. Rooney, A Facile green synthetic route for the preparation of highly active γ-Al2O3 from aluminum foil waste, Sci. Rep. 7 (1) (2017) 3593.
- aluminum foil waste, Sci. Rep. 7 (1) (2017) 3593.

 [50] V. Malinovschi, A.H. Marin, C. Ducu, S. Moga, V. Andrei, E. Coaca, V. Craciun, M. Lungu, C.P. Lungu, Improvement of mechanical and corrosion properties of commercially pure titanium using alumina PEO coatings, Coatings 12 (1) (2022)
- [51] R. Al-Oweini, H. El-Rassy, Synthesis and characterization by FTIR spectroscopy of silica aerogels prepared using several Si(OR)4 and R"Si(OR')3 precursors, J. Mol. Struct. 919 (1) (2009) 140–145.
- [52] R. Ellerbrock, M. Stein, J. Schaller, Comparing amorphous silica, short-rangeordered silicates and silicic acid species by FTIR, Sci. Rep. 12 (1) (2022) 11708.
- [53] M.P. Fernández-Liencres, A. Navarro, A. Ben Altabef, J.J. López-González, M. Fernández-Gómez, G.J. Kearley, Theoretical, ab initio and DFT, study of the structure and vibrational analysis of Raman, IR and INS spectra of (CH3)3SiNCO, Chem. Phys. 330 (1) (2006) 26–42.
- [54] G. Liu, L. Fu, A.V. Rode, V.S. Craig, Water droplet motion control on superhydrophobic surfaces: exploiting the Wenzel-to-Cassie transition, Langmuir 27 (6) (2011) 2595–2600.

- [55] Z. Cao, M.J. Stevens, J.-M.-Y. Carrillo, A.V. Dobrynin, Adhesion and wetting of soft nanoparticles on textured surfaces: transition between Wenzel and Cassie–Baxter states, Langmuir 31 (5) (2015) 1693–1703.
- [56] M. Liu, L. Jiang, Switchable adhesion on liquid/solid interfaces, Adv. Funct. Mater. 20 (21) (2010) 3753–3764.
- [57] R. David, A.W. Neumann, Energy barriers between the Cassie and Wenzel states on random, superhydrophobic surfaces, Colloids Surf. A Physicochem. Eng. Asp. 425 (2013) 51–58.
- [58] E. Rahimi, A. Rafsanjani-Abbasi, A. Kiani-Rashid, H. Jafari, A. Davoodi, Morphology modification of electrodeposited superhydrophobic nickel coating for enhanced corrosion performance studied by AFM, SEM-EDS and electrochemical measurements, Colloids Surf. A Physicochem. Eng. Asp. 547 (2018) 81–94.
- [59] X. Li, G. Wang, A.S. Moita, C. Zhang, S. Wang, Y. Liu, Fabrication of bio-inspired non-fluorinated superhydrophobic surfaces with anti-icing property and its wettability transformation analysis, Appl. Surf. Sci. 505 (2020) 144386.
- [60] X. Jiang, C. Zhou, J. Su, S. Tang, Enhanced anti-icing performance of novel superhydrophobic F-L@KH-SiO2/OTMS coating synergistic preparation with bionic micro-nano structures and modified nanoparticles, Chem. Eng. J. 498 (2024) 155264.
- [61] X. Li, Y. Wu, X. Lin, Z. Zhang, T. Hu, L. Jiang, T. Xiao, X. Tan, Eco-friendly fabrication of robust superhydrophobic coating with excellent anti-corrosion and anti-icing properties through using submillimeter particles as protective structure, Surf. Coat. Technol. 494 (2024) 131494.
- [62] Z. Lian, J. Zhou, Z. Liu, Y. Wan, R. Liu, J. Yang, J. Xu, Y. Tian, H. Yu, Hierarchically structured superhydrophobic surfaces with photothermal conversion to avoid icing, Int. J. Mech. Sci. 275 (2024) 109341.
- [63] P. Guo, Y. Zheng, M. Wen, C. Song, Y. Lin, L. Jiang, Icephobic/anti-icing properties of micro/nanostructured surfaces, Adv. Mater. 24 (19) (2012) 2642–2648.
- [64] K. Golovin, S.P.R. Kobaku, D.H. Lee, E.T. DiLoreto, J.M. Mabry, A. Tuteja, Designing durable icephobic surfaces, Sci. Adv. 2 (3) (2016) e1501496.

- [65] P. Irajizad, S. Nazifi, H. Ghasemi, Icephobic surfaces: Definition and figures of merit, Adv. Colloid Interface Sci. 269 (2019) 203–218.
- [66] Y. Wang, J. Zhang, H. Dodiuk, S. Kenig, J.A. Ratto, C. Barry, S. Turkoglu, J. Mead, The effect of superhydrophobic coating composition on the topography and ice adhesion, Cold Reg. Sci. Technol. 201 (2022) 103623.
- [67] L. Zhou, A. Liu, L. Zhou, Y. Li, J. Kang, J. Tang, Y. Han, H. Liu, Facilely Fabricated Self-Lubricated Photothermal Coating with Long-Term Durability and External-Replenishing Property for Anti-Icing/Deicing, ACS Appl. Mater. Interfaces 14 (6) (2022) 8537–8548.
- [68] C. Zhang, K. Pei, J. Zhao, Y. Zhou, S. Zhang, X. Han, Z. Guo, Hierarchical dandelion-like superhydrophobic surfaces with excellent stability and photothermal performance for efficient anti-/deicing, Chem. Eng. J. 510 (2025) 161582.
- [69] W. Wang, J. Chang, L. Chen, D. Weng, Y. Yu, Y. Hou, G. Yu, J. Wang, X. Wang, A laser-processed micro/nanostructures surface and its photothermal de-icing and self-cleaning performance, J. Colloid Interface Sci. 655 (2024) 307–318.
- [70] Y. Guo, H. Zhao, C. Zhang, G. Zhao, Super photothermal/electrothermal response and anti-icing/deicing capability of superhydrophobic multi-walled carbon nanotubes/epoxy coating, Chem. Eng. J. 497 (2024) 154383.
- [71] L. Zhang, B. Luo, K. Fu, C. Gao, X. Han, M. Zhou, T. Zhang, L. Zhong, Y. Hou, Y. Zheng, Highly Efficient Photothermal Icephobic/de-Icing MOF-Based Micro and Nanostructured Surface, Adv. Sci. 10 (34) (2023) 2304187.
- [72] X. He, X. Liu, J. Lu, H. Liu, Z. Wu, H. Xu, W. Tao, Z. Li, Facile fabrication of fluorine-free photo-thermal super-hydrophobic coating with hierarchical structure for efficient anti-icing and de-icing applications, Prog. Org. Coat. 194 (2024) 108543.
- [73] P. Atz-Dick, A. Konrath, Y. Rátiva Melo, C. Radtke, L.F.P. Dick, Aluminum anodizing with simultaneous silanization for increased hydrophobicity and corrosion protection, Appl. Surf. Sci. 593 (2022) 153392.